

## Spectral Characteristics of the He I D3 Line in a Quiescent Prominence Observed by THEMIS

Július Koza<sup>1</sup> · Ján Rybák<sup>1</sup> ·  
Peter Gömöry<sup>1</sup> · Matúš Kozák<sup>1</sup> ·  
Arturo López Ariste<sup>2,3</sup>

© Springer

**Abstract** We analyze the observations of a quiescent prominence acquired by the *Télescope Héliographique pour l'Étude du Magnétisme et des Instabilités Solaires* (THEMIS) in the He I 5876 Å (He I D3) multiplet aiming to measure the spectral characteristics of the He I D3 profiles and to find for them an adequate fitting model. The component characteristics of the He I D3 Stokes *I* profiles are measured by the fitting system approximating them with a double Gaussian. This model yields an He I D3 component peak intensity ratio of  $5.5 \pm 0.4$ , which differs from the value of 8 expected in the optically thin limit. Most of the measured Doppler velocities lie in the interval  $\pm 5 \text{ km s}^{-1}$ , with a standard deviation of  $\pm 1.7 \text{ km s}^{-1}$  around the peak value of  $0.4 \text{ km s}^{-1}$ . The wide distribution of the full-width at half maximum has two maxima at 0.25 Å and 0.30 Å for the He I D3 blue component and two maxima at 0.22 Å and 0.31 Å for the red component. The width ratio of the components is  $1.04 \pm 0.18$ . We show that the double-Gaussian model systematically underestimates the blue wing intensities. To solve this problem, we invoke a two-temperature multi-Gaussian model, consisting of two double-Gaussians, which provides a better representation of He I D3 that is free of the wing intensity deficit. This model suggests temperatures of 11.5 kK and 91 kK, respectively, for the cool and the hot component of the target prominence. The cool and hot components of a typical He I D3 profile have component peak intensity ratios of 6.6 and 8, implying a prominence geometrical width of 17 Mm and an optical thickness of 0.3 for the cool component, while the optical thickness of the hot component

---

✉ J. Koza  
koza@astro.sk

<sup>1</sup> Astronomical Institute, Slovak Academy of Sciences, Tatranská Lomnica, Slovakia

<sup>2</sup> Université de Toulouse, UPS-OMP, Institut de Recherche en Astrophysique et Planétologie, Toulouse, France

<sup>3</sup> CNRS, Institut de Recherche en Astrophysique et Planétologie, 14 Avenue Edouard Belin, F-31400 Toulouse, France

is negligible. These prominence parameters seem to be realistic, suggesting the physical adequacy of the multi-Gaussian model with important implications for interpreting He I D3 spectropolarimetry by current inversion codes.

**Keywords:** Prominences, Quiescent; Prominences, Dynamics

## 1. Introduction

The He I multiplet at 5876 Å, called the D3 line (hereafter He I D3), is one of the prime diagnostics used in ground-based observations of solar prominences (López Ariste, 2015). The multiplet consists of six transitions. In current solar spectropolarimetric observations, a combined emission of five transitions is resolved as its stronger blue component, while the sixth transition makes the weaker red component. Their spectral separation is 343.3 mÅ, giving the line its characteristic double-lobed profile. In the limiting case of negligible optical thickness in both components and the natural excitation of the triplet  $3^3D$  term, the blue-to-red ratio of the component peak intensities is 8:1 (Landi Degl’Innocenti, 1982).

The optical thinness of prominence plasma in He I D3 has been documented convincingly by i) the semi-empirical modeling of He I D3 profiles (Landman, Edberg, and Laney, 1977; Fontenla, 1979; Landman, 1981; Li, Gu, and Chen, 2000), ii) the non-LTE radiative modeling of He I D3 (Labrosse and Gouttebroze, 2001, 2004; Léger, 2008; Léger and Paletou, 2009), and iii) the obvious observational fact of the on-disk transparency of filaments in He I D3. The non-local thermal equilibrium (non-LTE) 2D multi-thread modeling by Léger (2008) and Léger and Paletou (2009) showed that under realistic conditions the prominence plasma never becomes optically thick for He I D3. Remarkably, these studies also showed that an optically thin structure, composed of several optically thin threads, emits the He I D3 profiles with component peak intensity ratios lower than 8. (We recommend a reader of Léger and Paletou (2009) to change their Figure 9 for Figure 7.21 in Léger (2008).) This compatibility of the optical thinness with the ratio of lower than 8 settles down earlier indications of non-negligible plasma optical thickness in He I D3 expressed in House and Smartt (1982); Athay *et al.* (1983); López Ariste and Casini (2002); Casini *et al.* (2003); and Wiehr and Bianda (2003) in the context of the observed ratios ranging from 6 to 7.6.

The He I D3 emission has been used mainly in spectropolarimetry of prominences aiming to measure prominence magnetic fields. The pioneering work in this field by Harvey and Tandberg-Hanssen (1968) was later followed by the series of studies by J. L. Leroy, V. Bommier, and S. Sahal-Bréchet (Leroy, 1989). The successful measurements made by these authors confirmed that the magnetic fields are essentially horizontal and twisted, with average field strengths of 10 – 20 G. Horizontal fields were detected in the majority of nearly 200 prominences observed from 2012 to 2015 (Levens *et al.*, 2016a). However, this study reported non-horizontal fields in a jet-like structure in an eruptive prominence, with inclinations tilted to 50° from the vertical. A recent multi-instrumental study

involving He I D3 by Levens *et al.* (2016b) reported finding a horizontal magnetic field in the legs of a tornado-like prominence. Schmieder *et al.* (2013) also found mostly horizontal magnetic fields by He I D3 in a prominence pillar showing signatures of magnetosonic waves propagating transverse to the magnetic field with a velocity of about  $10 \text{ km s}^{-1}$ , a period of about 300 s, and a wavelength of around 2000 km. The low signal-to-noise ratio of the He I D3 polarization signatures was interpreted in Schmieder *et al.* (2014) as a possible manifestation of a turbulent field superimposed on the macroscopic horizontal component of the prominence magnetic field. The results of these recent studies made use of He I D3 spectropolarimetry obtained by the *Télescope Héliographique pour l'Étude du Magnétisme et des Instabilités Solaires* (THEMIS) solar telescope.

Current models of prominences or filaments present them as aggregates of thin threads that are weakly or highly twisted into flux ropes with the effective volume-filling factor of radiating threads on the order of  $10^{-1} - 10^{-3}$  (Mackay *et al.*, 2010; Engvold, 2015). These models stem from high-resolution observations showing their fine-thread and knotty composition with thread widths down to the resolution limit of  $\approx 150 \text{ km}$  (Lin *et al.*, 2005, 2007; Lin, Martin, and Engvold, 2008; Heinzel and Anzer, 2006; Gunár *et al.*, 2007, 2008; Kuckein, Denker, and Verma, 2014; Freed *et al.*, 2016). A significant advance in modeling the fine structure of prominences and filaments has been achieved in the studies by Gunár and Mackay (2015a,b), which for the first time present the whole-prominence and filament fine-structure model and their synthetic  $H\alpha$  images in 3D. This study even presented the temporal evolution of prominences and filaments in response to changes in the underlying photospheric magnetic flux distribution, and it visualized their  $H\alpha$  appearance as it evolved in time. In an earlier study, Gunár *et al.* (2012) statistically tested the 2D multi-thread model of a quiescent prominence comparing the integrated intensity, the full-width at half maximum (hereafter FWHM or just the width), and the Doppler velocity of the observed and synthetic  $H\alpha$  profiles computed by the model. Of course, upcoming or future radiative transfer codes (see Štěpán *et al.*, 2015) and multi-thread models of prominences or filaments should allow the comparison of observed and synthetic He I D3 Stokes profiles. Léger (2008) and Léger and Paletou (2009) have presented the results of 2D non-LTE modeling of the He I D3 line taking the atomic fine structure of helium into account.

The aims of this study are twofold: first, to produce solid statistics of spectral characteristics of the blue and red component of He I D3 in a form that allows comparisons with future He I D3 modeling in the fashion applied in Gunár *et al.* (2012) for  $H\alpha$ ; second, to suggest an adequate fitting model for the He I D3 Stokes  $I$  profile in accord with contemporary views on prominence thermodynamic structure. The definition of these aims is motivated by a lack of pertinent studies.

## 2. Observations

A tree-like quiescent prominence occurring on 2 August 2014 at the east solar limb at the position angle of  $117^\circ$  (Figure 1) was selected as a target for the

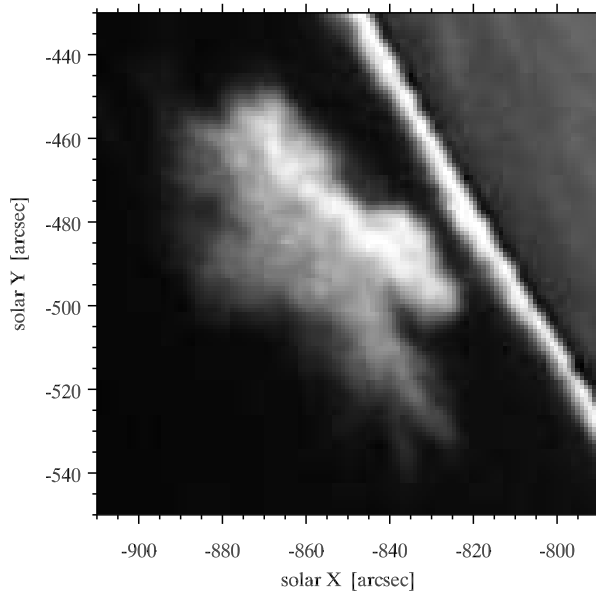


**Figure 1.** The cutout from the  $H\alpha$  broad-band full-disk image of the target prominence at the position angle of  $117^\circ$  obtained at the Kanzelhöhe Solar Observatory on 2 August 2014 at 14:12:39 UT. The THEMIS observation started at 14:59:02 UT. Different intensity scaling is applied to the disk and off-limb domain of the image.

double-beam spectropolarimetry in the He I D3 line by THEMIS operated in the MulTi Raies mode at Observatorio del Teide (López Ariste, Rayrole, and Semel, 2000). The prominence area in the plane of the sky, measured in the  $H\alpha$  broad-band image (Figure 1) taken at the Kanzelhöhe Solar Observatory (KSO, Pötzi *et al.*, 2015), is  $1483 \text{ Mm}^2$ . After subtracting the off-limb aureole that is due to the scattered photospheric light, the prominence relative intensity in the KSO  $0.7 \text{ \AA}$ -wide  $H\alpha$  Lyot filter with respect to the disk center is within the range from 7% to 27% with a median of 17%, corresponding to a radiance of  $1.0 \text{ W cm}^{-2} \text{ sr}^{-1}$ , and the prominence  $H\alpha$  radiant intensity is about  $3.9 \times 10^{22} \text{ W sr}^{-1}$ .

## 2.1. THEMIS Spectropolarimetry

The slit of the THEMIS spectrograph was opened to one arcsecond and placed parallel to the limb. The setup involved the Semel mask, *i.e.* a grid mask with three rectangular windows placed at the F1 focus of the telescope before the polarization analyzer (Semel, 1980; Briand and Ceppatelli, 2002). A rationale for its use and the necessity of 2D scanning in directions parallel ( $X$ ) and perpendicular ( $Y$ ) to the slit were clarified in Sainz Dalda and López Ariste (2007) and Schmieder *et al.* (2013). The 2D scanning of the target prominence started close to the limb at 14:59:02 UT and progressed radially away from the limb until about 17:00 UT. It involved one step in the  $X$  direction with the size of 15 arcsec followed by a step in the  $Y$  direction. In total, 25 steps separated by 2 arcsec were ordered in the  $Y$  direction. This provided a field

of view of  $88 \text{ arcsec} \times 50 \text{ arcsec}$ , and the top left panel of Figure 2 shows the effective cutout covering the whole target prominence. The axes keep the  $(X, Y)$  orientation defined above. Unlike Figure 1, in Figures 2, 3, 6, and 7, the solar disk and the target prominence are rotated about  $117^\circ$  clockwise (the THEMIS images; the image provided by the *Global Oscillation Network Group*  $H\alpha$  network monitor, operated by the *National Solar Observatory* (NSO/GONG); and the images taken by the *Atmospheric Imaging Assembly* onboard the *Solar Dynamic Observatory* (SDO/AIA)) or counterclockwise (the images taken by the *Solar TERrestrial RELations Observatory B* (STEREO B)) but keeping the same heliocentric coordinate system as in Figure 1. The STEREO B images were then flipped over around the  $Y$  axis. The white contour in the top left panel of Figure 2 outlines the prominence mask defined in Section 3.

One particular THEMIS spectrum at a given slit position is taken with the exposure time of 2 s, and overall, the observing procedure is the same as in Schmieder *et al.* (2013, 2014) and Levens *et al.* (2016a,b). We emphasize that in our case a modulation cycle of six images, spanning the three polarization states with either positive or negative signs, is repeated ten times to increase the signal-to-noise ratio. Therefore the 2D scanning lasts two hours. A typical acquisition time of four Stokes parameters at one slit position is 144 s, which includes the switch time of retarders and a dead time of the system duty cycle.

The spatial and spectral sampling of the obtained spectra is  $0.227 \text{ arcsec px}^{-1}$  and  $11.6 \text{ m}\text{\AA} \text{ px}^{-1}$ , respectively. The latter value is determined by the photospheric lines Fe I 5873.218  $\text{\AA}$  and Fe I 5877.797  $\text{\AA}$  that are seen in the spectra in the scattered photospheric light in the background (Figure 4). The dispersion of  $11.6 \text{ m}\text{\AA} \text{ px}^{-1}$  is used in calculating the spectral characteristics presented in Section 5 and in Figures 6 – 7.

Comparing the average Fe I line profiles with their counterparts extracted from the spectral atlas of solar disk-center intensity (Neckel, 1999) and convolved with a Gaussian, we estimate the instrumental smearing of the THEMIS spectra. We find that the smearing profile can be approximated by a Gaussian with FWHM = 71 m $\text{\AA}$ .

## 2.2. Morphology, Dynamics, and Evolution of the Target Prominence

To place the THEMIS observations in context, we make use of data provided by NSO/GONG (Harvey *et al.*, 2011), SDO/AIA (Lemen *et al.*, 2012; Pesnell, Thompson, and Chamberlin, 2012), and the *Extreme Ultraviolet Imager* (EUVI), which is a part of the *Sun-Earth Connection Coronal and Heliospheric Investigation* (SECCHI) instrument suite onboard the STEREO B spacecraft (Wuelser *et al.*, 2004; Wülser, Lemen, and Nitta, 2007; Howard *et al.*, 2008). Figure 2 and the movie available in the online edition show the slit-reconstructed map of the He I D3 peak intensity of the target prominence coaligned with the context images taken in the broad-band  $H\alpha$  filter of the NSO/GONG monitor at Observatorio del Teide and in the AIA 304  $\text{\AA}$  and 211  $\text{\AA}$  passbands during the THEMIS scanning overlaid with selected He I D3 peak intensity contours (yellow) and the  $H\alpha$  intensity contour (red). The coalignment of the He I D3 peak intensity

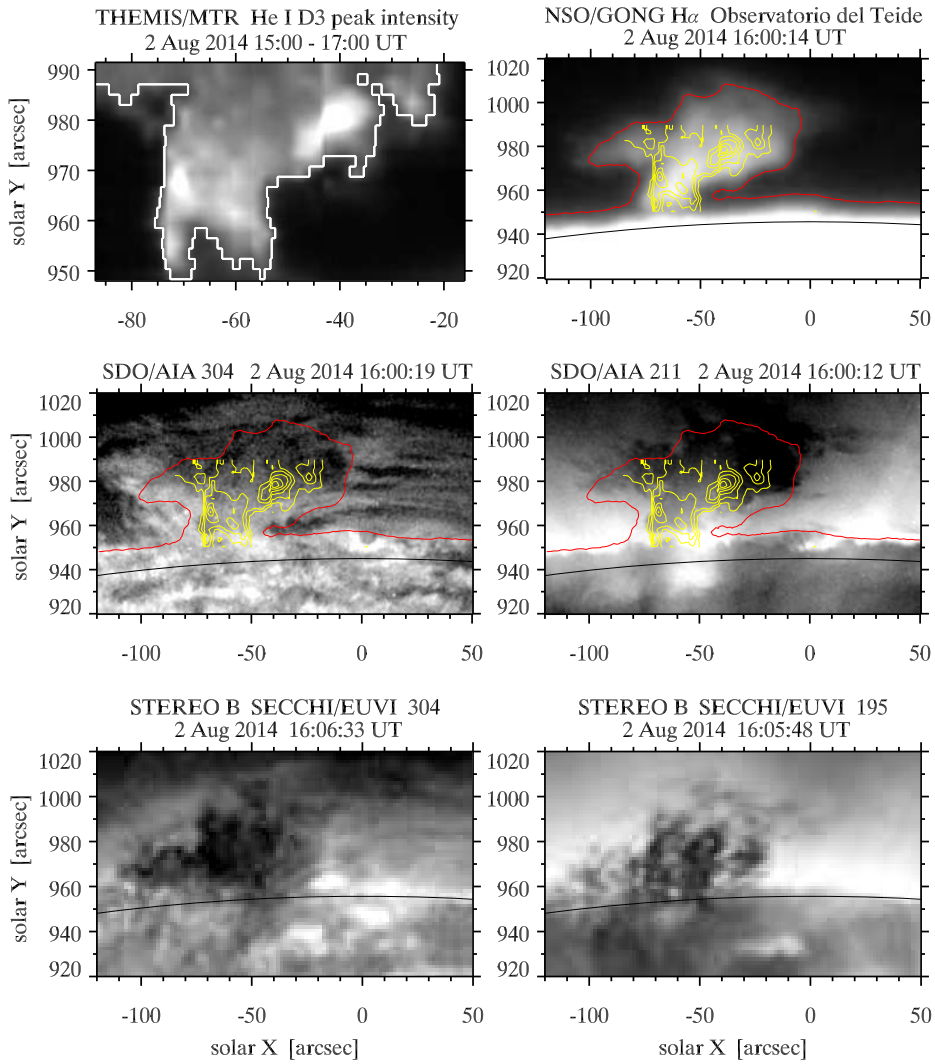


**Figure 2.** *Top left:* Slit-reconstructed map of the He I D3 peak intensity of the target prominence observed by THEMIS. The scanning ran from about 15:00 UT to 17:00 UT. The solar limb is out of the image below its lower border. Note the different fields of view of this and the following panels. The *contour* outlines the prominence mask applied to extract the data shown in Figures 6 – 8. *Top right:* The broad-band H $\alpha$  image of the prominence taken by the NSO/GONG network station at the Observatorio del Teide overplotted. The *red contour* marks the selected H $\alpha$  intensity level. The *yellow contours* show the coaligned He I D3 peak intensity of the prominence in the *left panel*. The *black arc* indicates the east photospheric limb. *Middle:* The SDO/AIA images of the prominence in the 304 Å (*left*) and 211 Å (*right*) passbands, respectively. The *contours* and the *black arcs* have the same meaning as in the *top right panel*. *Bottom:* STEREO B SECCHI/EUVI images of the prominence in the 304 Å (*left*) and 195 Å (*right*) passbands, respectively. The *black arc* indicates the west photospheric limb from the spacecraft viewpoint. The NSO/GONG H $\alpha$ , SDO/AIA, and SECCHI/EUVI images are taken approximately in the middle of scanning. The temporal evolution of the prominence in the NSO/GONG H $\alpha$  and in the SDO/AIA passbands during the scanning is shown in the movie that is available in the online edition. The movie is assembled from 120 frames with a temporal resolution of 1 min.

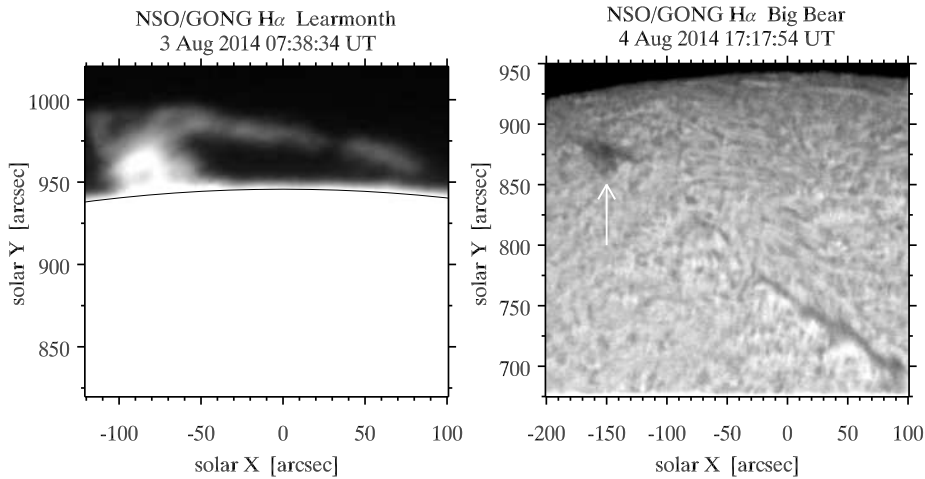


**Figure 3.** The broad-band  $H\alpha$  images of the target prominence on 3 August 2014 (*left*) and its probable on-disk filamentary counterpart on 4 August 2014 (*right*) marked by the *arrow*, taken at Learmonth and Big Bear NSO/GONG network stations, respectively. The *black arc* indicates the east photospheric limb.

image and the  $H\alpha$  image is approximate relying on morphological similarity. The coalignment of the  $H\alpha$  and AIA images is exact; it takes advantage of full-disk images and availability of all necessary data. The  $X$ -axis represents the position along the slit of the THEMIS spectrograph, and the  $Y$ -axis corresponds to the radial scanning direction. To highlight the structure of the target prominence, the top left panel shows a smaller field of view than the other panels. The He I D3 image suggests that the tree-like prominence consists of a central vertical pillar spreading out with height on both sides. The appearance of the prominence in  $H\alpha$  (top right panel) corresponds to the He I D3 peak intensity contours. The middle right panel shows the prominence in the AIA 211 Å passband as a dark structure against the bright background, absorbing the background coronal emission. Its “silhouette” agrees approximately with the shapes outlined by the He I D3 and  $H\alpha$  contours. However, the prominence appears very differently in the AIA 304 Å passband, which is shown in the middle left panel. It clearly illustrates the large areal extent and the horizontal arcades that stretch to the right, which are not visible in the previous panels.

Quiescent prominences are often characterized as sheets of plasma standing vertically above the polarity inversion line and showing fine horizontal or vertical threads (Orozco Suárez, Asensio Ramos, and Trujillo Bueno, 2014). The attained spatial resolution in the THEMIS and the NSO/GONG  $H\alpha$  observations prevents us from resolving any prominence fine structures. However, we do see signatures of strands in the AIA 211 Å and particularly in the 304 Å images. The bottom panels of the movie display plasma flows along the arcades, stretching to the right, that are generally parallel to the solar limb, similar to those described in Chae *et al.* (2008) and Orozco Suárez, Asensio Ramos, and Trujillo Bueno (2014). On the other side of the prominence body, one can see clumps of plasma flowing mostly toward the limb only in the AIA 304 Å passband.

To gain a comprehensive picture of the target prominence, we also inspect images taken by the STEREO A and B spacecraft on 2 August 2014 from 15:00 UT to 17:00 UT. While for STEREO A the prominence is invisible beyond the limb, the STEREO B images show it clearly at the west limb in all four passbands of the SECCHI/EUVI imager. Since the separation angle of the spacecraft with Earth is  $162^\circ$ , the SECCHI/EUVI 304 Å and 195 Å images of the prominence in the bottom panels of Figure 2 provide almost rear views of its dark central pillar and arcades stretching to the right, resembling its AIA 304 Å counterpart in the middle left panel. Different positions of the photospheric limbs in the SDO/AIA and STEREO B images are due to different solar disk diameters as seen from the vantage points of the spacecraft at heliocentric distances of about 1.015 AU and 1.003 AU, respectively.

The post-observation NSO/GONG H $\alpha$  image from 3 August 2014 in the left panel of Figure 3 shows that the prominence is still bright with a long and prominent arcade. The arrow in the NSO/GONG image from the following day (right panel) identifies its probable on-disk filamentary counterpart, which occupies a quiet-Sun area far from active regions. The SDO/HMI magnetogram (not shown here) suggests only an enhanced network in that area. Therefore, we classify the prominence as of quiescent type. It seems to be an isolated segment of the filament stretching diagonally from the lower right corner of the image. On that day, the marked structure disappears quickly.

### 3. Data Reduction

The primary reduction is the same as applied in Schmieder *et al.* (2013, 2014) and Levens *et al.* (2016a,b), and it involves data from all ten modulation cycles. The raw THEMIS spectra are reduced using the IDL package DeepStokes, whose main characteristics are outlined in López Ariste *et al.* (2009). The data reduction includes geometry corrections of inclination and curvature of spectral lines, dark current and bias subtraction, flat-field correction, and a careful handling of the polarization signals. Since the reduction yields Stokes  $Q$ ,  $U$ ,  $V$  profiles with very small amplitudes, typically 0.2 – 0.4% of the Stokes  $I$  peak intensity, we repeat the reduction taking data only from five modulation cycles as in Schmieder *et al.* (2013, 2014) and Levens *et al.* (2016a,b), but without improvement. Therefore, we aim the analysis only at the Stokes  $I$  profiles. To eliminate the large temporal smearing, we repeat the DeepStokes reduction again, but taking data at each slit position only from the fifth, *i.e.* only one modulation cycle, lasting about 14s. Figure 4 shows an example of the one-cycle Stokes  $I$  spectra.

To extract only prominence-relevant data, we construct the prominence mask as a vector of pixel subscripts with the Stokes  $I$  peak intensity  $I_{\max}$  greater than or equal to the *ad-hoc* threshold value  $0.2I_{\text{gmax}}$ , where  $I_{\text{gmax}}$  is the global maximum of the peak intensity over the whole prominence. The condition  $I_{\max} \geq 0.2I_{\text{gmax}}$  is fulfilled at the 2983 pixel positions defined in the top left panel of Figure 2 by the white contour representing the prominence in Figures 6 and 7. The data gaps due to the Semel mask (Figure 4) are filled in by linear interpolation.



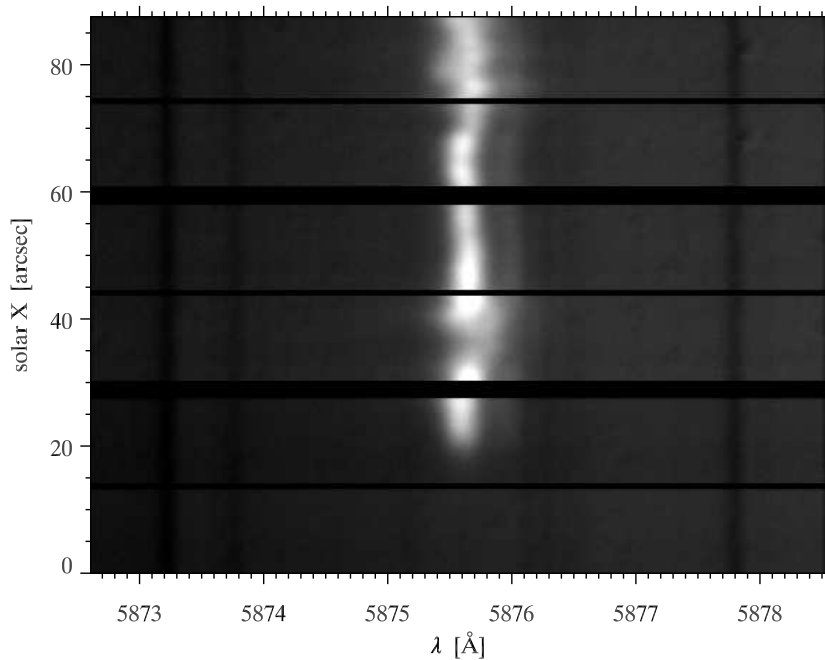


**Figure 4.** An example of the THEMIS spectrum showing He I D3 Stokes  $I$ , taken at the end of scanning when the slit is at  $Y = 990$  arcsec (the top left panel in Figure 2). The stronger blue component of He I D3 and its weaker red component are well resolved in the  $X$  span from 45 arcsec to 75 arcsec. The absorption features at about 5873.2 Å and 5877.8 Å, seen in the scattered continuum light, are the photospheric Fe I lines. The *black horizontal strips* are due to the Semel mask. The  $X$ -axis is parallel to the limb.

#### 4. Double-Gaussian Fit

Prominence models are often constructed and validated by comparing spectral characteristics of observed and synthetic line profiles (*e.g.* Gunár *et al.*, 2010; Schwartz, Gunár, and Curdt, 2015). The study by Gunár *et al.* (2012) made use of this approach in modeling the fine structure of a quiescent prominence by statistically comparing the Doppler velocity, the integrated intensity, and the FWHM of observed and synthetic  $H\alpha$  line profiles computed for an array of multi-thread prominence models. To provide solid statistics of spectral characteristics for the He I D3 Stokes  $I$  profiles, we perform a double-Gaussian fitting of their double-lobe structure resolved in the THEMIS spectra (Figure 4). The background intensity is approximated by a linear fit. The choice of this conservative fitting model is justified by the studies of, *e.g.*, House and Smartt (1982) and Landi Degl’Innocenti (1982), who claimed that the double Gaussian is an adequate representation of the He I D3 double-lobed profile.

For the background and double-Gaussian fitting we use the SolarSoft function `mpfitfun.pro` calling the engine `mpfit.pro` (Markwardt, 2009; Moré, 1978; Moré and Wright, 1993). The latter performs Levenberg-Marquardt least-squares minimization of the sum of the weighted squared differences between the data  $I_i$  ( $i = 1 \dots N$ ) and the user-supplied model function  $F_i$ . The relevant merit

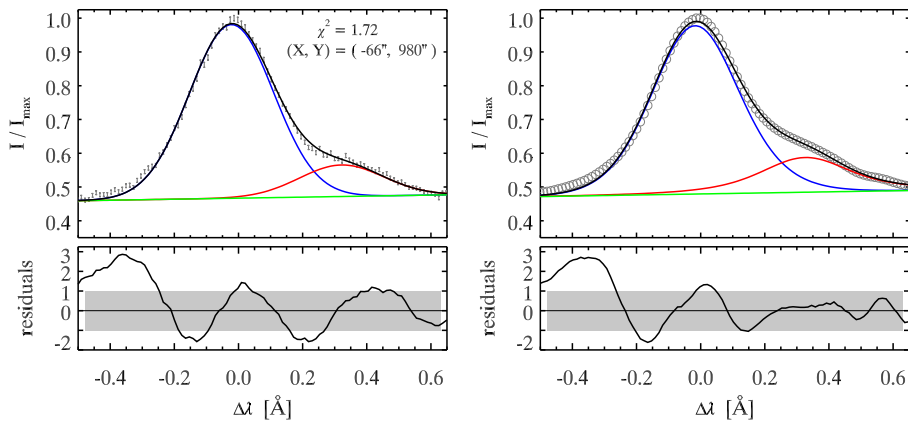


**Figure 5.** *Left:* An example of a typical double-Gaussian fit (*black*) of an observed He I D3 Stokes  $I$  profile (*gray error bars*) with a  $\chi^2$  value of 1.72. The blue and red Gaussian components and the linear background are represented by the *blue*, *red*, and *green* lines. *Right:* The averages of all 2983 profile fits (*black*), observations (*gray circles*), the blue and red Gaussian components, and the linear backgrounds. The *bottom subpanels* display the best-fit residuals expressed in the one-sigma unit shown as the shaded rectangle.

function is defined as  $\chi^2 = \frac{1}{N} \sum_{i=1}^N (I_i - F_i)^2 / \sigma_i^2$ , where the weights  $\sigma_i$  represent one-sigma uncertainties of the data. Assuming Poisson statistics for propagation of the uncertainties, we estimate these as the standard deviation of the background intensity variations  $\sigma_{\text{back}}$  outside the spectral lines and rescale them using the formula  $\sigma_i = \sigma_{\text{back}} \sqrt{I_i / \langle I_{\text{back}} \rangle}$ , where  $\sigma_i$  and  $I_i$  are the uncertainty and intensity at the particular wavelength and  $\langle I_{\text{back}} \rangle$  is the average background intensity outside the lines. The definition of the merit function implies that the  $\chi^2$  values of good fits are about one, meaning that the model is within the one-sigma uncertainties of the data.

We approximate the observed He I D3 Stokes  $I$  profiles with a model of two Gaussians superimposed on the first-order polynomial representing the background intensity. The model has seven free parameters: the peak intensities  $I_{\text{blue, red}}$ , the FWHM $_{\text{blue, red}}$ , the spectral position of the blue component peak  $\lambda_{\text{blue}}$ , and the two coefficients of the polynomial. The spectral position of the red component peak is tied to  $\lambda_{\text{blue}}$  as  $\lambda_{\text{red}} = \lambda_{\text{blue}} + 343.3 \text{ m}\text{\AA}$ . This coupling is kept in all models discussed below. We also check a six-parameter model with equal widths of the components. This model yields component peak intensity ratios that are different from the optically thin limit, suggesting radiative transfer effects. Therefore, we decide not to tie the widths and to adopt the seven-parameter model with the red component width as a free parameter.

Figure 5 shows an example of the fit of a typical profile and an average of all 2983 profile fits in the top left and right panels, respectively. The corresponding fit parameters are listed in columns 1 and 2 of Table 1. The bottom subpanels display the best-fit residuals  $(I_i - F_i) / \sigma_i$ , normalized by the uncertainties of observations  $\sigma_i$ . They show that the residuals of typical fits are mostly within the  $1\sigma$  span. The largest residuals of about  $3\sigma$  occur at  $\Delta\lambda \approx -0.35 \text{ \AA}$ , suggesting a systematic excess of the observed blue wing intensities over the Gaussian wing profile. We refer to this feature in the following as the blue wing excess.

## 5. Results of the Double-Gaussian Fitting

Figure 6 shows maps and histograms of  $\chi^2$  values and spectral characteristics of the observed double-lobed Stokes  $I$  profiles inferred by the double-Gaussian fitting of the one-cycle Stokes  $I$  profiles. The  $\chi^2$  distribution in the top left subpanel has a maximum and median at 1.2 and 1.8, respectively. Most of the measured Doppler velocities lie in the interval  $\pm 5 \text{ km s}^{-1}$ , and their distribution shows a redshifted median and peak at  $0.3 \text{ km s}^{-1}$  and  $0.4 \pm 1.7 \text{ km s}^{-1}$ , respectively. The latter value and its standard deviation result from the Gaussian fit of the distribution. An average of all 2983 pixel positions of blue component maxima is taken as a reference for the Doppler velocity.

The bottom panels of Figure 6 show maps of spatial distributions and histograms of the widths of the blue and red components. The maps of  $\text{FWHM}_{\text{blue}}$  and  $\text{FWHM}_{\text{red}}$  suggest a frequent occurrence of narrow profiles with component widths smaller than  $0.3 \text{ \AA}$  in a compact area in the center of the upper part of the prominence body at  $(X, Y) \approx (-55, 980) \text{ arcsec}$ . The area coincides approximately with a large island of redshifts in the velocity map. The  $\text{FWHM}_{\text{blue}}$  histogram has not one global maximum, but suggests a double-peaked distribution with two local maxima at  $0.25 \text{ \AA}$  and  $0.30 \text{ \AA}$ . Similarly, the distribution of  $\text{FWHM}_{\text{red}}$  has a prominent peak at  $0.22 \text{ \AA}$  and a second peak at  $0.31 \text{ \AA}$ . The medians of the  $\text{FWHM}_{\text{blue}}$  and  $\text{FWHM}_{\text{red}}$  histograms are at  $0.31 \text{ \AA}$  and  $0.29 \text{ \AA}$ , respectively. A comparison of the two histograms suggests an excess of red components narrower than  $0.23 \text{ \AA}$  and broader than  $0.48 \text{ \AA}$  compared with the blue components.

An indicator of the plasma optical thickness in He I D3 is the ratio of peak intensities and widths of the He I D3 double-lobed profile (Léger, 2008). The distribution of the peak intensity ratios in the lower left subpanel of Figure 7 has a median and peak at 5.4 and  $5.5 \pm 0.4$ , respectively. The latter value and its standard deviation result from the Gaussian fit of the distribution, which shows an excess of profiles with lower ratios down to 2. The distribution of the width ratios in the lower right subpanel has a median and peak at 1.03 and  $1.04 \pm 0.18$ .

We emphasize that the typical observed profile and its fit in the left panel of Figure 5 are chosen to be representative in the sense of typical values of  $\chi^2 = 1.72$ , a blue component width of  $0.31 \text{ \AA}$ , and a component peak intensity ratio of 5.5 (see also the corresponding entries in Tables 1 and 2).

Figure 8 presents pixel-by-pixel comparisons of the blue component peak intensities  $I_{\text{blue}}$  with the peak intensity ratios (left panel) and the width ratios (right panel) in the form of scatter plots supplementing the histograms in Figure 7. The plots suggest that while the weak profiles show a broad range of ratios, the strong profiles with high peak intensities  $I_{\text{blue}}$  have peak intensity ratios and width ratios of about  $5.5 \pm 0.4$  and  $1.04 \pm 0.18$ , respectively. These are indicated by the red vertical lines. The shape of the scatter plots also suggests that the values  $5.5 \pm 0.4$  and  $1.04 \pm 0.18$  inferred from the histograms in Figure 7 are representative of weak as well as strong profiles.

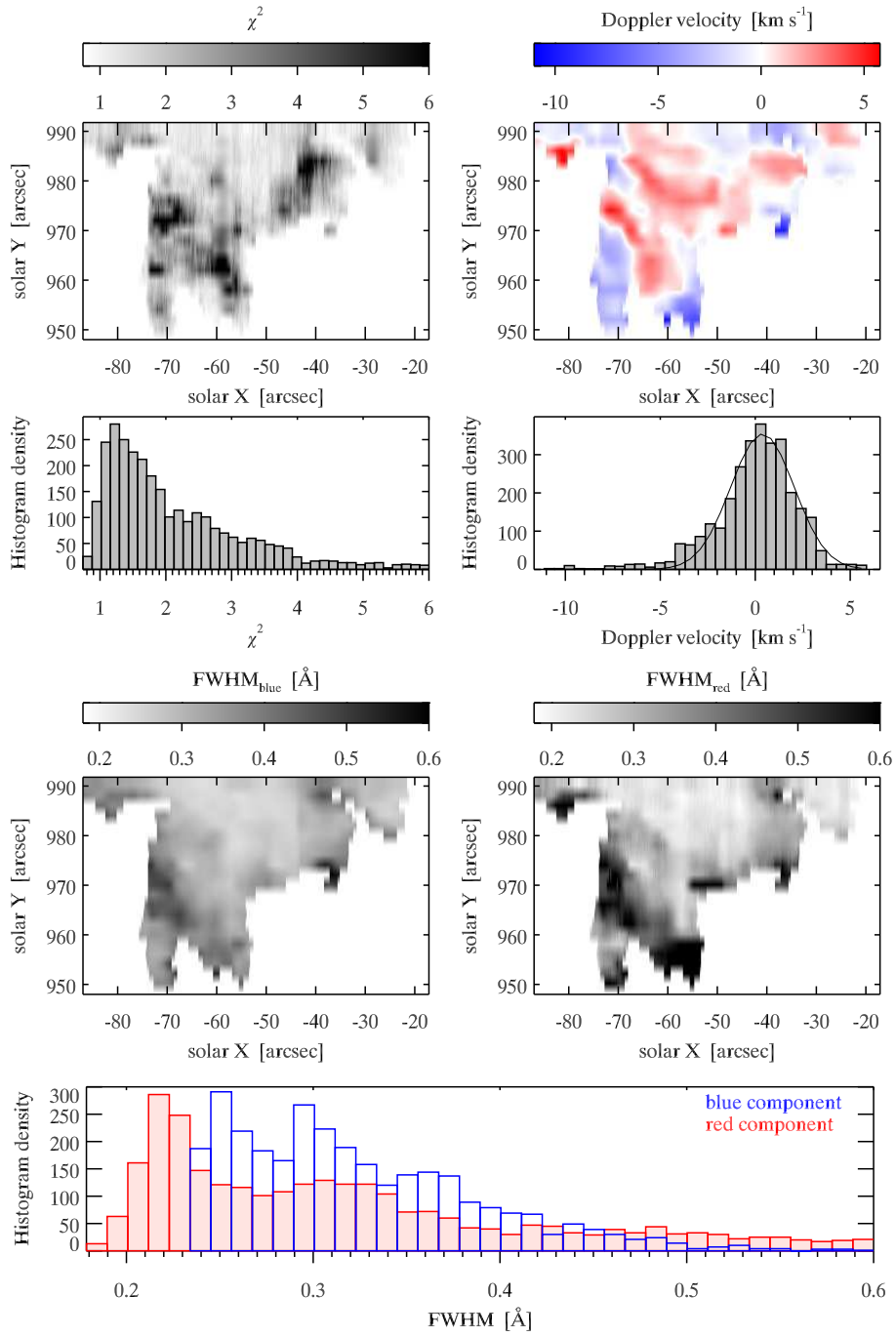


**Figure 6.** Maps and histograms of  $\chi^2$  values and spectral characteristics of the He I D3 line observed in the target prominence. *Top left:* The  $\chi^2$  values characterizing the best double-Gaussian fits. *Top right:* The Doppler velocity. The positive (*red*) is the redshift of the line center. The Gaussian fit of the histogram is indicated by the *thin line*. *Bottom:* FWHM of the blue (*left*) and the red (*right*) component of the He I D3 line.

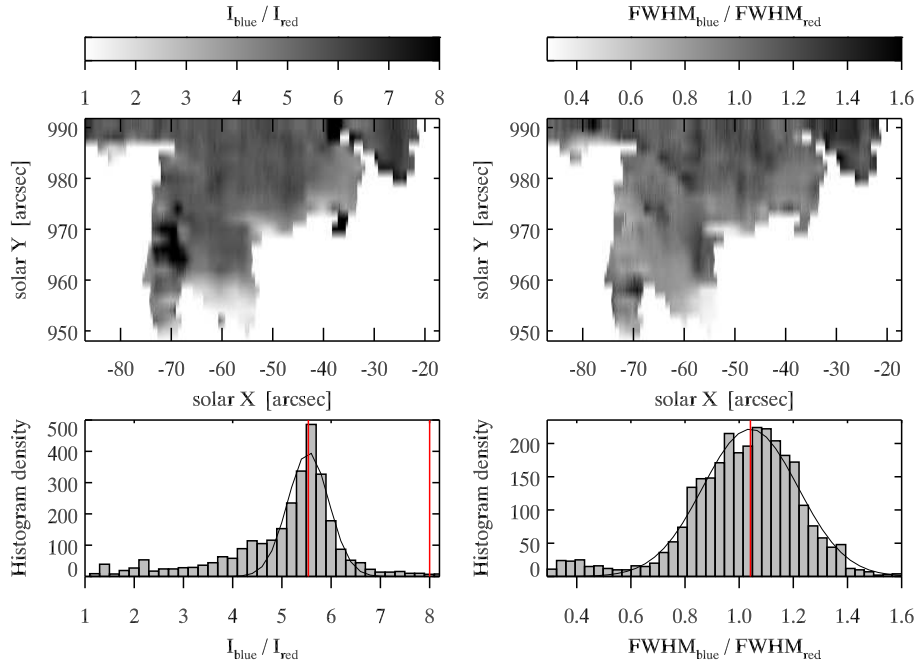


**Figure 7.** Ratios of the peak intensities  $I_{\text{blue}}/I_{\text{red}}$  (*left*) and the  $\text{FWHM}_{\text{blue}}/\text{FWHM}_{\text{red}}$  (*right*) of the blue and red components of the He I D3 line. The Gaussian fits of the histograms are indicated by the *thin lines*. The *red vertical lines* at 5.5 and 1.04 mark the peaks of the Gaussian fits. The *red line* at 8.0 indicates the value required by the optically thin limit.

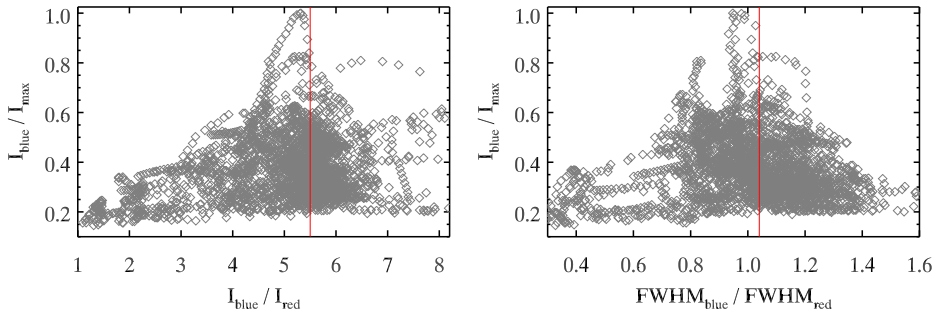


**Figure 8.** Scatter plots between measured quantities for all pixels within the target prominence. The He I D3 blue component peak intensity normalized to its maximum as a function of the ratios of the peak intensities  $I_{\text{blue}}/I_{\text{red}}$  (*left*) and the  $\text{FWHM}_{\text{blue}}/\text{FWHM}_{\text{red}}$  (*right*). The *red vertical lines* at 5.5 and 1.04 mark the values inferred from the histograms in Figure 7.

### 5.1. Effects of Temporal and Instrumental Smearing

To examine the effect of temporal smearing on the spectral characteristics of the target prominence, we calculate them using the ten-cycle Stokes  $I$  profiles with an effective integration time of 144 s. Since this trial yields the same results as those presented in Figures 6 and 7, we conclude that the dynamics of the target

quiescent prominence evolves on a timescale longer than two minutes at spatial scales larger than 2 arcsec.

The He I D3 profiles analyzed in this section are the convolutions of the original emission profiles with the instrumental profile of the THEMIS spectrograph, which can be approximated by a Gaussian with  $\text{FWHM} = 71 \text{ m}\text{\AA}$  (see Section 2.1). How much does this instrumental smearing bias the results? Could the smearing be responsible for the blue wing excess? To answer these questions, we deconvolve the typical He I D3 profile shown in the left panel of Figure 5 by applying the optimum filter (Brault and White, 1971). The deconvolved He I D3 profile is shown in the left panel of Figure 9 by the gray circles, and its fit is plotted with the black line. We apply the seven-parameter double-Gaussian model in fitting the deconvolved profile. Columns 1 and 3 of Table 1 compare the characteristics of the typical instrumentally smeared profile with the deconvolved profile. Apparently, the instrumental smearing may bias the results only insignificantly. Since the optimum filter removes noise, the bottom left subpanel of Figure 9 shows the differences  $\Delta I = 100(I_i - F_i)/I_i$ , where  $I_i$  represents the deconvolved data and  $F_i$  is the model function. The left subpanel of Figure 9 demonstrates that the blue wing excess persists even after deconvolving the typical profile, because the difference  $\Delta I$  at  $\Delta\lambda \approx -0.33 \text{ \AA}$  is 3.3%. Therefore we conclude that the blue wing excess is not due to the instrumental smearing. This might suggest inadequacy of the double-Gaussian model in representing the typical He I D3 profiles emitted by the target prominence.

## 6. Alternative Fitting Models

In this study we adopt the double-Gaussian fitting model of the He I D3 profiles. An indicator that the fitting model is inadequate is not only the value of  $\chi^2$ , but also the shape of residuals. If a model represents data correctly, then the residuals or differences  $\Delta I$  should be featureless with no systematic structure other than random excursions reflecting the noise variations. However, the residuals in Figure 5 and differences in the left subpanel of Figure 9 are not featureless, because they show quasi-periodic variations, which are particularly apparent in the blue wing of the blue component at  $\Delta\lambda \approx -0.35 \text{ \AA}$ . This may indicate an inadequacy of the adopted seven-parameter double-Gaussian model. The blue wing excess is also apparent in the He I D3 Stokes  $I$  profiles shown in Landman, Edberg, and Laney (1977); House and Smartt (1982); López Ariste and Casini (2002, 2003); Casini *et al.* (2003, 2009); and López Ariste and Aulanier (2007). Therefore, in the following we examine alternative He I D3 fitting models with the aim to propose a new model that appears to be characterized by small and featureless differences  $\Delta I$  and negligible blue wing excess as well.

### 6.1. Double-Lorentzian Model

Recently, González Manrique *et al.* (2016) applied a double-Lorentzian profile in fitting blended components of the He I 10 830  $\text{\AA}$  triplet observed by the *GREGOR Infrared Spectrograph* (GRIS) at the 1.5-meter GREGOR solar telescope.

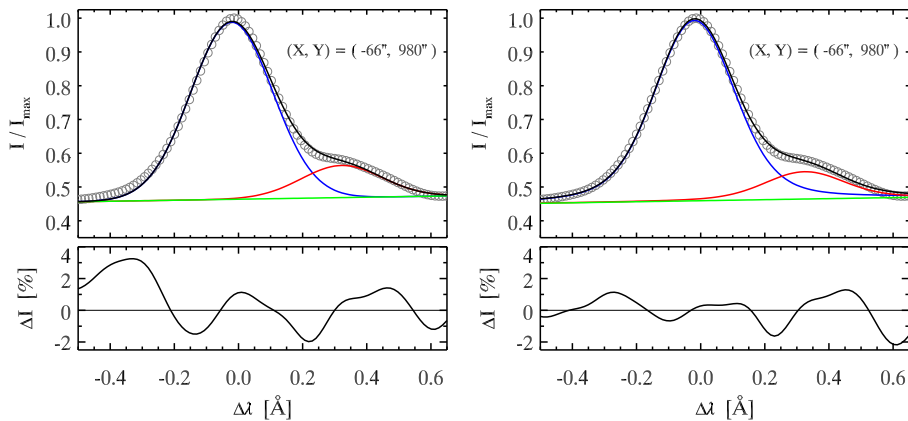


**Figure 9.** The double-Gaussian and the double-Voigt fits (*black lines* in the *left and right panels*, respectively) of the deconvolved He I D3 Stokes  $I$  profile (*gray circles*) shown in the left panel of Figure 5. The blue and red fit components and the linear background are represented by the *blue, red, and green lines*. The *bottom subpanels* display the differences between the deconvolved He I D3 profile and the fits.

Following this approach, we test the seven-parameter double-Lorentzian model using the typical profile shown in the left panel of Figure 5. For this particular profile, the model renders much higher  $\chi^2$  values and residuals than the seven-parameter double-Gaussian model. Moreover, it substantially overestimates the observed blue wing intensity of the blue component at  $\Delta\lambda \approx -0.35 \text{ \AA}$ . Hence, the double-Lorentzian model renders an inadequate representation of our data and is dismissed.

## 6.2. Double-Voigt Model

Since the double Gaussian underestimates and the double Lorentzian overestimates the observed blue wing intensity of the blue component, the double-Voigt function might render a natural compromise. In fact, the Voigt function has been employed by Elste (1953) and Landman, Edberg, and Laney (1977) in fitting the He I D3 profiles. Therefore, we test a model consisting of two Voigt functions normalized to their maxima. The model has seven free parameters: the peak amplitudes  $I_{\text{blue, red}}$ ; the damping parameter  $\Gamma$  and FWHM common for both components; the spectral position of the blue component peak  $\lambda_{\text{blue}}$ ; and two coefficients of the polynomial. The parameters of this model for the typical deconvolved profile are given in column 4 of Table 1. The inferred damping parameter is shown there both in wavelength units as  $\Gamma_\lambda$  and in frequency units as the decadic logarithm of  $\Gamma_\nu$ . They are linked by the conversion formula  $\Gamma_\nu = c\Gamma_\lambda/\lambda^2$ , where  $c$  is the speed of light and  $\lambda$  is the wavelength of He I D3. The right panel of Figure 9 shows the typical deconvolved He I D3 profile by the gray circles, and its double-Voigt fit is represented by the black line. The bottom subpanel illustrates that the model is free of the blue wing excess, compared with the left subpanel and subpanels in Figure 5, and renders a satisfactory fit with featureless differences  $\Delta I$  smaller than 2%. Although the model seems to comply

**Table 1.** Parameters of fitting models shown in Figures 5, 9, and 10. Types of fitting models and profiles in particular columns are given below the table. Equal FWHM and  $T$  are assumed for components of the double-Voigt fit. Columns 5 and 6 list the parameters of the cool and hot component (in parentheses) of the multi-Gaussian fit.

Spectral characteristic	1	2	3	4	5	6
FWHM <sub>blue</sub> [ Å ]	0.31	0.32	0.30			
FWHM <sub>red</sub> [ Å ]	0.31	0.35	0.30	0.25	0.28 (0.65)	0.26 (0.56)
$I_{\text{blue}}/I_{\text{max}}$	–	–	–	–	0.94 (0.52)	0.86 (0.60)
$T$ [ kK ]	–	–	–	–	11.5 (91)	9 (65)
Peak intensity ratio	5.5	4.9	5.5	6.6	6.6 (8.0)	6.3 (4.1)
Width ratio	1.0	0.9	1.0	1.0	1.0 (1.0)	1.0 (1.0)
$\Gamma_{\lambda}$ [ Å ]/ $\log(\Gamma_{\nu}$ [s <sup>-1</sup> ])	–	–	–	0.5/10.6	–	–

- 1 Double-Gaussian fit of the typical smeared profile, the left panel of Figure 5.
- 2 Double-Gaussian fit of the average smeared profile, the right panel of Figure 5.
- 3 Double-Gaussian fit of the typical deconvolved profile, the left panel of Figure 9.
- 4 Double-Voigt fit of the typical deconvolved profile, the right panel of Figure 9.
- 5 Multi-Gaussian fit of the typical deconvolved profile, the left panel of Figure 10.
- 6 Multi-Gaussian fit of the average deconvolved profile, the right panel of Figure 10.

with our requirements imposed on a new adequate model, we postpone a final judgement about its physical adequacy to Section 7.3.1 of the Discussion.

### 6.3. Multi-Gaussian Model

The problem of the enhanced wing emissions in the He I D3 and He I 10830 Å lines was addressed by Landman, Edberg, and Laney (1977) and Kotrc and Heinzel (1989), who invoked two-temperature models of prominence structure. Inspired by this approach to explain the surplus of blue wing emission, we construct a multi-Gaussian model consisting of two double-Gaussians with different line widths representing the cool and hot components of a prominence. The model has nine free parameters: the peak intensities of the blue components  $I_{\text{blue}}$  (two parameters); the ratios of the peak intensities  $I_{\text{blue}}/I_{\text{red}}$  constrained by the limit values 0.001 and 8 (two parameters); the FWHM common for the blue and red components, but different for the cool and hot ones (two parameters); the spectral position of the blue component peak  $\lambda_{\text{blue}}$  (one parameter); and two coefficients of the polynomial (two parameters). The parameters of this model for the typical and average deconvolved profiles are listed in columns 5 and 6 of Table 1, showing the hot component parameters in parentheses. It also shows the blue component intensities  $I_{\text{blue}}/I_{\text{max}}$  and the kinetic temperatures  $T$  of the cool and hot components estimated by the formula:

$$T = \frac{m_{\text{He}}}{2k} \left\{ \left( \frac{\text{FWHM } c}{2\sqrt{\ln 2} \lambda} \right)^2 - v^2 \right\}, \quad (1)$$

where  $m_{\text{He}}$  is the mass of a helium atom,  $k$  is the Boltzmann constant,  $c$  is the speed of light,  $\lambda$  is the wavelength of He I D3, and  $v$  is the microturbulent



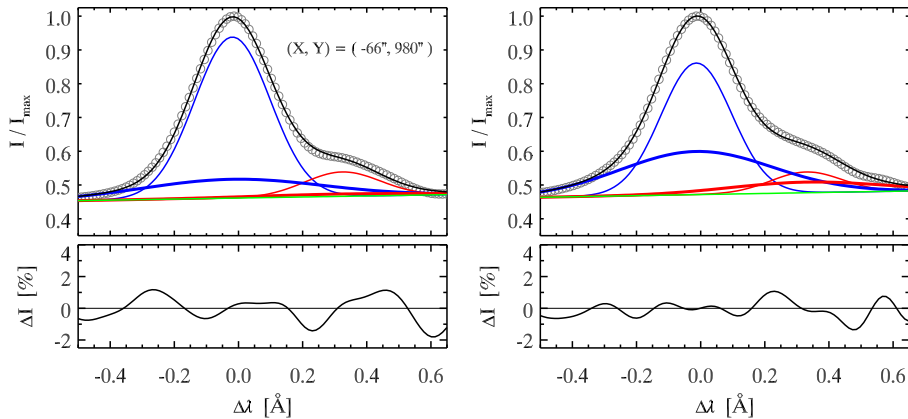


**Figure 10.** The multi-Gaussian fits (*black lines*) of the typical He I D3 Stokes  $I$  profile (*left*) and the average profile (*right*) shown by the *gray circles*. Instrumental smearing of the profiles is deconvolved by the optimum filter. The *thin blue and thin red lines* correspond to the cool component and the thick lines to the hot component. The *bottom subpanels* display the differences between the deconvolved profiles and their fits.

velocity of  $5 \text{ km s}^{-1}$  for both components (*e.g.* Gouttebroze, Heinzel, and Vial, 1993; Léger and Paletou, 2009).

Figure 10 displays the typical and average He I D3 profiles free of the instrumental smearing by the gray circles and their multi-Gaussian fits, comprising the cool (thin blue and red lines) and hot components (thick lines), shown by the black lines. The bottom subpanels illustrate that the model is free of the blue wing excess when compared with respective subpanels in Figures 5 and 9, and renders satisfactory fits with differences  $\Delta I$  smaller than 2%, similar to the double-Voigt model. Thus, the multi-Gaussian model also complies with the requirements we impose on our new fitting model. We postpone a final judgement about its physical adequacy to Section 7.3.2 of the following Discussion.

## 7. Discussion

### 7.1. Small Stokes $Q$ , $U$ , $V$ Amplitudes

An important fact characterizing the target prominence is the surprisingly small amplitude of the Stokes  $Q$ ,  $U$ ,  $V$  profiles, typically about 0.2 – 0.4% of the Stokes  $I$  peak intensities. The previous studies by, *e.g.*, Landi Degl’Innocenti (1982); Querfeld *et al.* (1985); López Ariste and Casini (2002, 2003); Casini *et al.* (2003, 2009); Ramelli and Bianda (2005); López Ariste and Aulanier (2007); and Paletou (2008) reported the Stokes  $Q$ ,  $U$ ,  $V$  amplitudes ranging from  $4 \times 10^{-3} \%$  to 2.3%. Is the weak polarimetric signal a possible consequence of some inherent feature of this particular target prominence? Or is it rather due to non-optimal seeing, some technical aspects of the instrument setup, and/or an inadequate observing or reduction procedure? An inadequacy of the observing or reduction procedure may probably be excluded, because decreasing the number of modulation cycles adopted for the data reduction from ten to five, as used in Schmieder

**Table 2.** Statistics of the He I D3 spectral characteristics of the quiescent prominence derived from the histograms in Figures 6 and 7. The positive velocity indicates redshift of the He I D3 line center. The location of the second peak in the distributions of  $\text{FWHM}_{\text{blue}}$  and  $\text{FWHM}_{\text{red}}$  is shown in parentheses.

Spectral characteristic	Median	Peak location	Sigma
Doppler velocity [ $\text{km s}^{-1}$ ]	0.3	0.4	1.7
$\text{FWHM}_{\text{blue}}$ [ $\text{\AA}$ ]	0.31	0.25 (0.30)	–
$\text{FWHM}_{\text{red}}$ [ $\text{\AA}$ ]	0.29	0.22 (0.31)	–
Component peak intensity ratio	5.4	5.5	0.4
Component width ratio	1.03	1.04	0.18

*et al.* (2013, 2014) and Levens *et al.* (2016a,b), does not bring improvement. A very plausible explanation was suggested by López Ariste and Casini (2003). To quote them: “It has been suggested by Querfeld *et al.* (1985) that line-of-sight integration or limited spatial resolution might result in a depression of the degree of linear polarization of the observed radiation, which would be wrongly interpreted in terms of Hanle depolarization by stronger fields.” Therefore, we conclude that a combination of non-optimal seeing, the long integration time, and THEMIS instrumental characteristics very probably caused a degradation of the spatial resolution. This is most likely the culprit for the small Stokes  $Q$ ,  $U$ ,  $V$  amplitudes.

## 7.2. Spectral Characteristics of the Double-Gaussian Model

While Table 1 lists the spectral characteristics of the typical and average He I D3 profile inferred by three different fitting models, Table 2 summarizes statistics of the He I D3 spectral characteristics derived from the histograms in Figures 6 and 7, which represent the double-Gaussian model.

The most important fact characterizing the target prominence is the component peak intensity ratio of  $5.5 \pm 0.4$  (Table 2), which differs from the optically thin limit 8. However, this is not a new finding. House and Smartt (1982) previously reported a peak ratio of  $6.6 \pm 0.4$ . In a study of eight prominences, Athay *et al.* (1983) found the He I D3 peak intensity ratios ranging from 6.1 to 7.6. Finally, López Ariste and Casini (2002) and Wiehr and Bianda (2003) reported peak intensity ratios of 6.8 and 6, respectively. While the former two studies employed the double-Gaussian model, the method of inferring the ratios in the latter two articles is unclear. Thus, the measured peak intensity ratio of  $5.5 \pm 0.4$  is on the lower limit of the values reported so far.

Many of the published Doppler velocity measurements of prominences were made in  $\text{H}\alpha$  by the MSDP instrument (Mein, 1977, 1991), but reports on the He I D3 velocity measurements are infrequent. A search of the NASA Astrophysics Data System provides us only with the study by Prasad, Ambastha, and Mathew (1999), presenting the line-of-sight velocity distribution over a quiescent prominence observed in He I D3 with a standard deviation of  $1.8 \text{ km s}^{-1}$ . This

agrees with the deviation of  $1.7 \text{ km s}^{-1}$  derived from our measurements. The interval of  $\pm 5 \text{ km s}^{-1}$ , presented in the top right panel of Figure 6, is characteristic for the quiescent type of prominences and is fully in line with He I D3 (Prasad, Ambastha, and Mathew, 1999),  $\text{H}\alpha$  (*e.g.* Schmieder *et al.*, 2010), He I 10830 Å (*e.g.* Orozco Suárez, Asensio Ramos, and Trujillo Bueno, 2014), and Mg II k & h (*e.g.* Vial *et al.*, 2016) Doppler-velocity measurements in quiescent prominences.

The sharp lower limit of the measured width  $\text{FWHM}_{\text{blue}}$  of the dominant He I D3 blue component at about  $0.23 \text{ \AA}$  (the bottom panel of Figure 6) agrees well with the lower limit of Doppler widths of He I D3 reported by Athay *et al.* (1983). However, they reported the upper limit of the observed FWHM at  $0.32 \text{ \AA}$ , while the histogram in the bottom panel of Figure 6 shows a continuous distribution of broad profiles beyond this value. House and Smartt (1982) measured a nearly equal FWHM of  $0.28 \text{ \AA}$  for both components. Similarly, the median of 15 FWHM values reported in Landman, Edberg, and Laney (1977, Table 1) was  $0.27 \text{ \AA}$ . Most of the He I D3 FWHMs measured by Prasad, Ambastha, and Mathew (1999) were within the interval from  $0.32 \text{ \AA}$  to  $0.56 \text{ \AA}$ , in good agreement with our results shown in the bottom panel of Figure 6.

Finally, we find width ratios of the He I D3 blue and red components of  $1.04 \pm 0.18$  over almost the entire prominence. Their close equality was also reported by House and Smartt (1982) and Athay *et al.* (1983). The width equality is a strong confirmation that the He I D3 multiplet components in the plasma have a common origin.

### 7.3. Toward a New Fitting Model

In the following we examine in detail the physical adequacy of the double-Voigt model and the multi-Gaussian model as alternative models of He I D3.

#### 7.3.1. Double-Voigt Model

We have shown that the double-Voigt model of the typical profile requires a damping parameter  $\Gamma_\lambda = 0.5 \text{ \AA}$  corresponding to  $\log(\Gamma_\nu [\text{s}^{-1}]) = 10.6$ . How does this observed value compare with the theoretical parameter given as the sum of the natural damping parameter  $\Gamma_{\text{RAD}}$  and the collisional (or Van der Waals) damping parameter  $\Gamma_{\text{VDW}}$  (*e.g.* Rutten, 2003)? The latter parameter represents collisions of the emitting helium atoms with the neutral hydrogen atoms. The sum of the relevant Einstein coefficients of spontaneous emission  $A$ , adopted from the National Institute of Standards and Technology Atomic Spectra Database (NIST ASD, Kramida *et al.*, 2016), gives the value  $\log(\Gamma_{\text{RAD}} [\text{s}^{-1}]) = 7.7$ . Assuming a prominence gas pressure of  $1 \text{ dyn cm}^{-2}$  and a temperature of  $11 \text{ kK}$  in combination with the line-broadening theory by Warner (1967), one can estimate for He I D3 the value of  $\log(\Gamma_{\text{VDW}} [\text{s}^{-1}]) = 4.4$ . Thus, the observed damping parameter is about three orders of magnitudes larger than the theoretical parameter. Apparently, this disqualifies the double-Voigt model from any further consideration because it is physical inadequate. This conclusion is in accord with Landman, Edberg, and Laney (1977), who also dismissed the

physical adequacy of the Voigt-shaped absorption coefficient for He I D3. They inferred the broadening parameter

$$a = \frac{2\sqrt{\ln 2}}{\text{FWHM}} \frac{\lambda^2}{c} \frac{\Gamma_\nu}{4\pi} \quad (2)$$

on the order of magnitude 0.1 corresponding to  $\log(\Gamma_\nu [\text{s}^{-1}]) = 10.3$  for  $\text{FWHM} = 0.27 \text{ \AA}$ . Because this value was also orders of magnitude greater than the values calculated on the basis of commonly accepted prominence plasma parameters, they ruled out collisional broadening as a realistic solution of the blue wing excess. This is in accord with Landi Degl'Innocenti and Landolfi (2004, p. 712 in Volume II), who claimed that collisions can be neglected in forming He I D3.

### 7.3.2. Multi-Gaussian Model

Focusing on the typical He I D3 profile (the left panel of Figure 10 and column 5 in Table 1), we assess the multi-Gaussian model, which is similar to the two-temperature model of He I D3 applied in Landman, Edberg, and Laney (1977) and Landman (1981). The medians of 32 FWHM values, reported in Table 2 of the latter study for the cool and hot components, are about  $0.22 \text{ \AA}$  and  $0.59 \text{ \AA}$ , respectively, and thus smaller than the equivalent FWHMs  $0.28 \text{ \AA}$  and  $0.65 \text{ \AA}$  inferred by the typical profile. Remarkably, the temperatures 11.5 kK and 91 kK of the cool and hot components of the multi-Gaussian model agree very well with the central and boundary temperatures of 10 kK and 100 kK for the 2D model of prominence fine structure applied in Gunár *et al.* (2007) and Schwartz, Gunár, and Curdt (2015). This may be evidence of the physical adequacy of the multi-Gaussian model.

While the component peak intensity ratio of 8 of the hot component (Table 1) implies its negligible optical thickness, the ratio of 6.6 of the cool component can be interpreted in terms of the prominence geometrical width and optical thickness based on the 2D multi-thread prominence model by Léger (2008). Figures 7.21 and 7.22 in Léger (2008) present the He I D3 component peak intensity ratio as a function of the number of 1.2 Mm wide prominence threads and their total optical thickness for the temperatures 8 kK and 17 kK. Taking the temperature 11.5 kK of the cool component of the target prominence and the ratio of 6.6, one can estimate by interpolating the values in these figures that the target prominence is composed from of 14 threads with a total geometrical width of 17 Mm and an optical thickness of 0.3. Remarkably, the width, corresponding to 23 arcsec, is comparable with the typical width of a filament (see the right panel of Figure 3). However, the optical thickness of 0.3 is about an order of magnitude greater than the thicknesses reported in Landman, Edberg, and Laney (1977); Landman (1981); and Li, Gu, and Chen (2000). In this context, Landman, Edberg, and Laney (1977) commented on their method and results by stating: “The computed line shapes are relatively insensitive to the  $\tau_{0i}$  because of the smallness of these quantities.” For this reason, we may conclude that the prominence parameters inferred by the typical profile support the physical adequacy of the multi-Gaussian model with important implications for the interpretation of He I D3 spectropolarimetry by current inversion codes.

## 8. Summary and Conclusions

In this study we analyze the observations of a quiescent, tree-like prominence scanned by the THEMIS spectrograph on 2 August 2014 in the He I D3 multiplet. In a broad-band H $\alpha$  image the distribution of its relative intensity with respect to the disk center has the median at 17%.

The double-Gaussian model of the He I D3 Stokes  $I$  profiles shows wide distributions of the FWHM with two maxima at 0.25 Å and 0.30 Å for the He I D3 blue component and at 0.22 Å and 0.31 Å for the red component. The FWHM distributions have medians at 0.31 Å and 0.29 Å for the blue and red component, respectively. We find width ratios of the He I D3 components of  $1.04 \pm 0.18$  over almost over the entire prominence. The width equality is a strong confirmation of the common origin of the multiplet components in the plasma. This model yields a He I D3 component peak intensity ratio of  $5.5 \pm 0.4$ , which differs from the value of 8 expected in the optically thin limit. Most of the measured Doppler velocities are from the interval  $\pm 5 \text{ km s}^{-1}$  with a standard deviation of  $\pm 1.7 \text{ km s}^{-1}$  around the peak value of  $0.4 \text{ km s}^{-1}$  (Section 5). The pixel-by-pixel comparisons of the He I D3 spectral characteristics in Figure 8 and their values in Tables 1 and 2 may become valuable in future modeling of He I D3. However, we have shown that the double-Gaussian model fails to reproduce the observed He I D3 blue wing intensities and leads to quasi-periodic residuals with more than one-sigma amplitudes (Section 4).

We demonstrate that the blue wing excess persists even after correcting the typical He I D3 profile for the instrumental profile of the THEMIS spectrograph, suggesting the inadequacy of the double-Gaussian model (Section 5.1). To investigate this issue we test the double-Lorentzian and the double-Voigt model showing that the former produces unsatisfactory fits and the latter is physically invalid (Sections 6.1, 6.2, and 7.3.1).

With the goal of identifying an adequate fitting model, we examine the multi-Gaussian model consisting of two double-Gaussians with different line widths, representing the cool and hot components of the prominence. This model adequately reproduces the typical He I D3 profile, indicating temperatures for the cool and hot components of about 11.5 kK and 91 kK, respectively. The cool and hot components of the typical He I D3 profile have component peak intensity ratios of 6.6 and 8, implying a prominence geometrical width of 17 Mm and an optical thickness of 0.3 for the cool component, while the optical thickness of the hot component is negligible (Sections 6.3 and 7.3.2). These prominence parameters seem to be realistic, which supports the physical adequacy of the multi-Gaussian model. This has important implications for the interpretation of He I D3 spectropolarimetry using current inversion codes.

These conclusions are based on data taken during a non-optimal seeing period, which is most likely the culprit for the observed small amplitudes of the Stokes  $Q$ ,  $U$ ,  $V$  profiles, which typically reach only 0.2 – 0.4% of the Stokes  $I$  peak intensities (Sections 3 and 7.1). A statistically larger sample of data, taken under more favorable seeing conditions, is needed to confirm these conclusions.

**Acknowledgments** We thank an anonymous referee for valuable comments, which improved the article substantially. J. Koza is grateful to P. Heinzel and E. Džifčáková for fruitful

discussions, comments, and suggestions. J. Koza and M. Kozák would like to thank B. Gelly, the director of the THEMIS solar telescope, and the technical team for their support during their THEMIS observing campaign. The authors thank M. Saniga for language corrections of the article. This work was supported by the Science Grant Agency project VEGA 2/0004/16. The THEMIS observations were taken within the EU-7FP-SOLARNET Transnational Access and Service Programme (High Resolution Solar Physics Network - FP7-INFRASTRUCTURES-2012-1). This article was created by the realization of the project ITMS No. 26220120029, based on the supporting operational Research and development program financed from the European Regional Development Fund. This work uses GONG data obtained by the NSO Integrated Synoptic Program (NISP), managed by the National Solar Observatory, which is operated by the Association of Universities for Research in Astronomy (AURA), Inc. under a cooperative agreement with the National Science Foundation. The AIA data used here are courtesy of SDO (NASA) and the AIA consortium. The STEREO B data used here were produced by an international consortium of the Naval Research Laboratory (USA), Lockheed Martin Solar and Astrophysics Lab (USA), NASA Goddard Space Flight Center (USA), Rutherford Appleton Laboratory (UK), University of Birmingham (UK), Max-Planck-Institut für Solar System Research (Germany), Centre Spatiale de Liege (Belgium), Institut d'Optique Theorique et Appliquee (France), and Institut d'Astrophysique Spatiale (France). This research has made use of NASA Astrophysics Data System.

**Disclosure of Potential Conflicts of Interest** The authors declare that they have no conflicts of interest.

## References

- Athay, R.G., Querfeld, C.W., Smartt, R.N., Landi Degl'Innocenti, E., Bommier, V.: 1983, Vector magnetic fields in prominences. III - He I D3 Stokes profile analysis for quiescent and eruptive prominences. *Solar Phys.* **89**, 3. ADS.
- Braut, J.W., White, O.R.: 1971, The Analysis and Restoration of Astronomical Data via the Fast Fourier Transform. *Astron. Astrophys.* **13**, 169. ADS.
- Briand, C., Ceppatelli, G.: 2002, THEMIS: instrumentation, results and perspectives. In: Sawaya-Lacoste, H. (ed.) *SOLMAG 2002. Proceedings of the Magnetic Coupling of the Solar Atmosphere Euroconference, ESA Special Publication* **505**, 11. ADS.
- Casini, R., López Ariste, A., Tomczyk, S., Lites, B.W.: 2003, Magnetic Maps of Prominences from Full Stokes Analysis of the He I D3 Line. *Astrophys. J. Lett.* **598**, L67. ADS.
- Casini, R., López Ariste, A., Paletou, F., Léger, L.: 2009, Multi-Line Stokes Inversion for Prominence Magnetic-Field Diagnostics. *Astrophys. J.* **703**, 114. ADS.
- Chae, J., Ahn, K., Lim, E.-K., Choe, G.S., Sakurai, T.: 2008, Persistent Horizontal Flows and Magnetic Support of Vertical Threads in a Quiescent Prominence. *Astrophys. J. Lett.* **689**, L73. ADS.
- Elste, G.: 1953, Die Entzerrung von Spektrallinien unter Verwendung von Voigtfunktionen. Mit 8 Textabbildungen. *ZAp* **33**, 39. ADS.
- Engvold, O.: 2015, Description and Classification of Prominences. In: Vial, J.-C., Engvold, O. (eds.) *Solar Prominences, Astrophysics and Space Science Library* **415**, 31. ADS.
- Fontenla, J.M.: 1979, A prominence model based on spectral observations. *Solar Phys.* **64**, 177. ADS.
- Freed, M.S., McKenzie, D.E., Longcope, D.W., Wilburn, M.: 2016, Analysis of Flows inside Quiescent Prominences as Captured by Hinode/Solar Optical Telescope. *Astrophys. J.* **818**, 57. ADS.
- González Manrique, S.J., Kuckein, C., Pastor Yabar, A., Collados, M., Denker, C., Fischer, C.E., Gómory, P., Diercke, A., Bello González, N., Schlichenmaier, R., Balthasar, H., Berkefeld, T., Feller, A., Hoch, S., Hofmann, A., Kneer, F., Lagg, A., Nicklas, H., Orozco

- Suárez, D., Schmidt, D., Schmidt, W., Sigwarth, M., Sobotka, M., Solanki, S.K., Soltau, D., Staude, J., Strassmeier, K.G., Verma, M., Volkmer, R., von der Lühe, O., Waldmann, T.: 2016, Fitting peculiar spectral profiles in He I 10830Å absorption features. *Astronomische Nachrichten* **337**, 1057. ADS.
- Gouttebroze, P., Heinzel, P., Vial, J.C.: 1993, The hydrogen spectrum of model prominences. *Astron. Astrophys. Suppl.* **99**, 513. ADS.
- Guñar, S., Mackay, D.H.: 2015a, 3D Whole-Prominence Fine Structure Modeling. *Astrophys. J.* **803**, 64. ADS.
- Guñar, S., Mackay, D.H.: 2015b, 3D Whole-prominence Fine Structure Modeling. II. Prominence Evolution. *Astrophys. J.* **812**, 93. ADS.
- Guñar, S., Heinzel, P., Schmieder, B., Schwartz, P., Anzer, U.: 2007, Properties of prominence fine-structure threads derived from SOHO/SUMER hydrogen Lyman lines. *Astron. Astrophys.* **472**, 929. ADS.
- Guñar, S., Heinzel, P., Anzer, U., Schmieder, B.: 2008, On Lyman-line asymmetries in quiescent prominences. *Astron. Astrophys.* **490**, 307. ADS.
- Guñar, S., Schwartz, P., Schmieder, B., Heinzel, P., Anzer, U.: 2010, Statistical comparison of the observed and synthetic hydrogen Lyman line profiles in solar prominences. *Astron. Astrophys.* **514**, A43. ADS.
- Guñar, S., Mein, P., Schmieder, B., Heinzel, P., Mein, N.: 2012, Dynamics of quiescent prominence fine structures analyzed by 2D non-LTE modelling of the H $\alpha$  line. *Astron. Astrophys.* **543**, A93. ADS.
- Harvey, J.W., Tandberg-Hanssen, E.: 1968, The magnetic field in some prominences measured with the He I, 5876 Å line. *Solar Phys.* **3**, 316. ADS.
- Harvey, J.W., Bolding, J., Clark, R., Hauth, D., Hill, F., Kroll, R., Luis, G., Mills, N., Purdy, T., Henney, C., Holland, D., Winter, J.: 2011, Full-disk Solar H-alpha Images From GONG. In: *AAS/Solar Physics Division Abstracts #42*, *Bulletin of the American Astronomical Society* **43**, 17.45. ADS.
- Heinzel, P., Anzer, U.: 2006, On the Fine Structure of Solar Filaments. *Astrophys. J. Lett.* **643**, L65. ADS.
- House, L.L., Smartt, R.N.: 1982, Vector magnetic fields in prominences. I - Preliminary discussion of polarimeter observations in He I D3. *Solar Phys.* **80**, 53. ADS.
- Howard, R.A., Moses, J.D., Vourlidas, A., Newmark, J.S., Socker, D.G., Plunkett, S.P., Korendyke, C.M., Cook, J.W., Hurley, A., Davila, J.M., Thompson, W.T., St Cyr, O.C., Mentzell, E., Mehalick, K., Lemen, J.R., Wuelser, J.P., Duncan, D.W., Tarbell, T.D., Wolfson, C.J., Moore, A., Harrison, R.A., Waltham, N.R., Lang, J., Davis, C.J., Eyles, C.J., Mapson-Menard, H., Simnett, G.M., Halain, J.P., Defise, J.M., Mazy, E., Rochus, P., Mercier, R., Ravet, M.F., Delmotte, F., Auchere, F., Delaboudiniere, J.P., Bothmer, V., Deutsch, W., Wang, D., Rich, N., Cooper, S., Stephens, V., Maahs, G., Baugh, R., McMullin, D., Carter, T.: 2008, Sun Earth Connection Coronal and Heliospheric Investigation (SECCHI). *Space Sci. Rev.* **136**, 67. ADS.
- Kotrc, P., Heinzel, P.: 1989, Analysis of HeI 10830 Line in a Quiescent Prominence. *Hvar Observatory Bulletin* **13**, 371. ADS.
- Kramida, A., Yu. Ralchenko, Reader, J., and NIST ASD Team: 2016, NIST Atomic Spectra Database (ver. 5.4), [Online]. Available: <http://physics.nist.gov/asd> [2017, January 11]. National Institute of Standards and Technology, Gaithersburg, MD.
- Kuckein, C., Denker, C., Verma, M.: 2014, High-resolution spectroscopy of a giant solar filament. In: Schmieder, B., Malherbe, J.-M., Wu, S.T. (eds.) *Nature of Prominences and their Role in Space Weather*, *IAU Symposium* **300**, 437. ADS.
- Labrosse, N., Gouttebroze, P.: 2001, Formation of helium spectrum in solar quiescent prominences. *Astron. Astrophys.* **380**, 323. ADS.
- Labrosse, N., Gouttebroze, P.: 2004, Non-LTE Radiative Transfer in Model Prominences. I. Integrated Intensities of He I Triplet Lines. *Astrophys. J.* **617**, 614. ADS.
- Landi Degl'Innocenti, E.: 1982, The determination of vector magnetic fields in prominences from the observations of the Stokes profiles in the D3 line of helium. *Solar Phys.* **79**, 291. ADS.
- Landi Degl'Innocenti, E., Landolfi, M. (eds.): 2004, *Polarization in Spectral Lines*, *Astrophysics and Space Science Library* **307**. ADS.
- Landman, D.A.: 1981, Quiescent prominence spectrophotometry - Sodium D1,2, helium D3, and calcium /plus/ lambda 8498. *Astrophys. J.* **251**, 768. ADS.
- Landman, D.A., Edberg, S.J., Laney, C.D.: 1977, Measurements of H $\beta$ , He D $_3$ , and Ca $^+$   $\lambda$ 8542 line emission in quiescent prominences. *Astrophys. J.* **218**, 888. ADS.

- Léger, L.: 2008, Transfert de rayonnement hors-etl multidimensionnel. application au spectre de l'hélium des protuberances solaires. PhD thesis, Planète et Univers [physics]. Université Paul Sabatier - Toulouse III, 2008. Français. <https://tel.archives-ouvertes.fr/tel-00332781/document>.
- Léger, L., Paletou, F.: 2009, 2D non-LTE radiative modelling of He I spectral lines formed in solar prominences. *Astron. Astrophys.* **498**, 869. ADS.
- Lemen, J.R., Title, A.M., Akin, D.J., Boerner, P.F., Chou, C., Drake, J.F., Duncan, D.W., Edwards, C.G., Friedlaender, F.M., Heyman, G.F., Hurlburt, N.E., Katz, N.L., Kushner, G.D., Levay, M., Lindgren, R.W., Mathur, D.P., McFeaters, E.L., Mitchell, S., Rehse, R.A., Schrijver, C.J., Springer, L.A., Stern, R.A., Tarbell, T.D., Wuelser, J.-P., Wolfson, C.J., Yanari, C., Bookbinder, J.A., Cheimets, P.N., Caldwell, D., Deluca, E.E., Gates, R., Golub, L., Park, S., Podgorski, W.A., Bush, R.I., Scherrer, P.H., Gummie, M.A., Smith, P., Auken, G., Jerram, P., Pool, P., Souffri, R., Windt, D.L., Beardsley, S., Clapp, M., Lang, J., Waltham, N.: 2012, The Atmospheric Imaging Assembly (AIA) on the Solar Dynamics Observatory (SDO). *Solar Phys.* **275**, 17. ADS.
- Leroy, J.L.: 1989, Observation of prominence magnetic fields. In: Priest, E.R. (ed.) *Dynamics and Structure of Quiescent Solar Prominences*, *Astrophysics and Space Science Library* **150**, 77. ADS.
- Levens, P.J., Schmieder, B., López Ariste, A., Labrosse, N., Dalmasse, K., Gelly, B.: 2016a, Magnetic Field in Atypical Prominence Structures: Bubble, Tornado, and Eruption. *Astrophys. J.* **826**, 164. ADS.
- Levens, P.J., Schmieder, B., Labrosse, N., López Ariste, A.: 2016b, Structure of Prominence Legs: Plasma and Magnetic Field. *Astrophys. J.* **818**, 31. ADS.
- Li, K., Gu, X., Chen, X.: 2000, Calculations and physical properties of the D3 emission lines of a prominence. *Mon. Not. Roy. Astron. Soc.* **313**, 761. ADS.
- Lin, Y., Martin, S.F., Engvold, O.: 2008, Filament Substructures and their Interrelation. In: Howe, R., Komm, R.W., Balasubramaniam, K.S., Petrie, G.J.D. (eds.) *Subsurface and Atmospheric Influences on Solar Activity*, *Astronomical Society of the Pacific Conference Series* **383**, 235. ADS.
- Lin, Y., Engvold, O., Rouppe van der Voort, L., Wiik, J.E., Berger, T.E.: 2005, Thin Threads of Solar Filaments. *Solar Phys.* **226**, 239. ADS.
- Lin, Y., Engvold, O., Rouppe van der Voort, L.H.M., van Noort, M.: 2007, Evidence of Traveling Waves in Filament Threads. *Solar Phys.* **246**, 65. ADS.
- López Ariste, A.: 2015, Magnetometry of Prominences. In: Vial, J.-C., Engvold, O. (eds.) *Solar Prominences*, *Astrophysics and Space Science Library* **415**, 179. ADS.
- López Ariste, A., Aulanier, G.: 2007, Unveiling the Magnetic Field Topology of Prominences. In: Heinzel, P., Dorotović, I., Rutten, R.J. (eds.) *The Physics of Chromospheric Plasmas*, *Astronomical Society of the Pacific Conference Series* **368**, 291. ADS.
- López Ariste, A., Casini, R.: 2002, Magnetic Fields in Prominences: Inversion Techniques for Spectropolarimetric Data of the He I D<sub>3</sub> Line. *Astrophys. J.* **575**, 529. ADS.
- López Ariste, A., Casini, R.: 2003, Improved Estimate of the Magnetic Field in a Prominence. *Astrophys. J. Lett.* **582**, L51. ADS.
- López Ariste, A., Rayrole, J., Semel, M.: 2000, First results from THEMIS spectropolarimetric mode. *Astron. Astrophys. Suppl.* **142**, 137. ADS.
- López Ariste, A., Asensio Ramos, A., Manso Sainz, R., Derouich, M., Gelly, B.: 2009, Variability of the polarization profiles of the Ba II D<sub>2</sub> line in the solar atmosphere. *Astron. Astrophys.* **501**, 729. ADS.
- Mackay, D.H., Karpen, J.T., Ballester, J.L., Schmieder, B., Aulanier, G.: 2010, Physics of Solar Prominences: II - Magnetic Structure and Dynamics. *Space Sci. Rev.* **151**, 333. ADS.
- Markwardt, C.B.: 2009, Non-linear Least-squares Fitting in IDL with MPFIT. In: Bohlender, D.A., Durand, D., Dowler, P. (eds.) *Astronomical Data Analysis Software and Systems XVIII*, *Astronomical Society of the Pacific Conference Series* **411**, 251. ADS.
- Mein, P.: 1977, Multi-channel subtractive spectrograph and filament observations. *Solar Phys.* **54**, 45. ADS.
- Mein, P.: 1991, Solar 2D spectroscopy - A new MSDP instrument. *Astron. Astrophys.* **248**, 669. ADS.
- Moré, J.: 1978, The Levenberg-Marquardt Algorithm: Implementation and Theory. In: Watson, G.A. (ed.) *Numerical Analysis, Lecture Notes in Mathematics* **630**, 105.
- Moré, J., Wright, S.: 1993, *Optimization software guide*, *Frontiers in Applied Mathematics* **14**. ISBN 978-0-89871-322-0.



- Neckel, H.: 1999, Announcement Spectral Atlas of Solar Absolute Disk-Averaged and Disk-Center Intensity from 3290 to 12510 Å (Brault and Neckel, 1987) now Available from Hamburg Observatory Anonymous FTP Site. *Solar Phys.* **184**, 421.
- Orozco Suárez, D., Asensio Ramos, A., Trujillo Bueno, J.: 2014, The magnetic field configuration of a solar prominence inferred from spectropolarimetric observations in the He I 10 830 Å triplet. *Astron. Astrophys.* **566**, A46. ADS.
- Paletou, F.: 2008, The magnetic field of solar prominences. In: Charbonnel, C., Combes, F., Samadi, R. (eds.) *SF2A-2008*, 559. ADS.
- Pesnell, W.D., Thompson, B.J., Chamberlin, P.C.: 2012, The Solar Dynamics Observatory (SDO). *Solar Phys.* **275**, 3. ADS.
- Pötzi, W., Veronig, A.M., Riegler, G., Amerstorfer, U., Pock, T., Temmer, M., Polanec, W., Baumgartner, D.J.: 2015, Real-time Flare Detection in Ground-Based H $\alpha$  Imaging at Kanzelhöhe Observatory. *Solar Phys.* **290**, 951. ADS.
- Prasad, C.D., Ambastha, A., Mathew, S.K.: 1999, Dynamical properties of quiescent prominence in He D3 5876 Å line emission. *Bulletin of the Astronomical Society of India* **27**, 411. ADS.
- Querfeld, C.W., Smartt, R.N., Bommier, V., Landi Degl'Innocenti, E., House, L.L.: 1985, Vector magnetic fields in prominences. II - He I D3 Stokes profiles analysis for two quiescent prominences. *Solar Phys.* **96**, 277. ADS.
- Ramelli, R., Bianda, M.: 2005, He-D<sub>3</sub> polarization observed in prominences. In: Hanslmeier, A., Veronig, A., Messerotti, M. (eds.) *Solar Magnetic Phenomena, Astrophysics and Space Science Library* **320**, 215. ADS.
- Rutten, R.J.: 2003, *Radiative Transfer in Stellar Atmospheres*. ADS.
- Sainz Dalda, A., López Ariste, A.: 2007, Chromospheric reversals in the emergence of an ephemeral region. *Astron. Astrophys.* **469**, 721. ADS.
- Schmieder, B., Chandra, R., Berlicki, A., Mein, P.: 2010, Velocity vectors of a quiescent prominence observed by Hinode/SOT and the MSDP (Meudon). *Astron. Astrophys.* **514**, A68. ADS.
- Schmieder, B., Kucera, T.A., Knizhnik, K., Luna, M., Lopez-Ariste, A., Toot, D.: 2013, Propagating Waves Transverse to the Magnetic Field in a Solar Prominence. *Astrophys. J.* **777**, 108. ADS.
- Schmieder, B., Tian, H., Kucera, T., López Ariste, A., Mein, N., Mein, P., Dalmasse, K., Golub, L.: 2014, Open questions on prominences from coordinated observations by IRIS, Hinode, SDO/AIA, THEMIS, and the Meudon/MSDP. *Astron. Astrophys.* **569**, A85. ADS.
- Schwartz, P., Gunár, S., Curdt, W.: 2015, Non-LTE modelling of prominence fine structures using hydrogen Lyman-line profiles. *Astron. Astrophys.* **577**, A92. ADS.
- Semel, M.: 1980, A precise optical polarization analyzer. *Astron. Astrophys.* **91**, 369. ADS.
- Štěpán, J., Trujillo Bueno, J., Leenaarts, J., Carlsson, M.: 2015, Three-dimensional Radiative Transfer Simulations of the Scattering Polarization of the Hydrogen Ly $\alpha$  Line in a Magnetohydrodynamic Model of the Chromosphere-Corona Transition Region. *Astrophys. J.* **803**, 65. ADS.
- Vial, J.-C., Pelouze, G., Heinzel, P., Kleint, L., Anzer, U.: 2016, Observed IRIS Profiles of the h and k Doublet of Mg II and Comparison with Profiles from Quiescent Prominence NLTE Models. *Solar Phys.* **291**, 67. ADS.
- Warner, B.: 1967, Some Effects of Pressure Broadening in Solar and Stellar Curves of Growth. *Mon. Not. Roy. Astron. Soc.* **136**, 381. ADS.
- Wiehr, E., Bianda, M.: 2003, Solar prominence polarimetry. *Astron. Astrophys.* **404**, L25. ADS.
- Wueller, J.-P., Lemen, J.R., Tarbell, T.D., Wolfson, C.J., Cannon, J.C., Carpenter, B.A., Duncan, D.W., Gradwohl, G.S., Meyer, S.B., Moore, A.S., Navarro, R.L., Pearson, J.D., Rossi, G.R., Springer, L.A., Howard, R.A., Moses, J.D., Newmark, J.S., Delaboudiniere, J.-P., Artzner, G.E., Auchere, F., Bougnet, M., Bouyries, P., Bridou, F., Clotaire, J.-Y., Colas, G., Delmotte, F., Jerome, A., Lamare, M., Mercier, R., Mullet, M., Ravet, M.-F., Song, X., Bothmer, V., Deutsch, W.: 2004, EUVI: the STEREO-SECCHI extreme ultraviolet imager. In: *Telescopes and Instrumentation for Solar Astrophysics*, *Society of Photo-Optical Instrumentation Engineers (SPIE) Conference Series* **5171**, 111. ADS.
- Wueller, J.-P., Lemen, J.R., Nitta, N.: 2007, The STEREO SECCHI/EUVI EUV coronal imager. In: *Solar Physics and Space Weather Instrumentation II*, *Society of Photo-Optical Instrumentation Engineers (SPIE) Conference Series* **6689**, 668905. ADS.